Additively Manufactured Wideband Low-Profile Bidirectional 2-D Beam-Scanning Antenna Using Double Folded Transmitarrays With Curved Polarizers

Zhenjun Zhai, Feng Lin, *Senior Member, IEEE*, Yang Yang, *Senior Member, IEEE*, and Houjun Sun

***Abstract*—This paper presents a wideband low-profile bidirectional two-dimensional (2-D) beam-scanning antenna for millimeter-wave applications. It achieves independently controlled bidirectional beams by two orthogonally mirrored folded transmitarrays (TAs) overlapping in space, significantly reducing the antenna profile. The folded TA consists of a feed source, a curved polarizer and a receive-transmit (R-T) array. The feed source is realized by an all-metal wideband miniaturized magnetoelectric (ME) dipole based on the metal 3D-printing technique. The curved metal grating acts as a polarizer, which achieves reflection and transmission for y-polarized and *x*-polarized waves, respectively. Using the additively manufactured electronics (AME) technique, the R-T array element is realized by two wideband tightly coupled bow-tie dipole antennas connected by a pair of differential microstrip-line phase shifters with true-time delay and continuous 360° tuning range. Finally, 2-D beam scanning with constant beam direction across the operation band is achieved by adjusting the polarizer along the *x*- and y-directions. The height diameter ratio (*H*/*D*) is 0.5, while the measured 2-D bidirectional beam scanning range covers ±10° in both the E- and H-planes within 27 ~ 39 GHz, with a maximum scan loss of 1.9 dB. The measured peak gain is 27.1 dBi, and the maximum aperture efficiency is 53.4%. The measured 1-dB and 3-dB overlapped gain bandwidths for 0° and 180° beams are 30 ~ 36.2 GHz (18.7%) and 27~40 GHz (38.8%), respectively.**

***Index Terms*—millimeter-wave, wideband, folded transmitarray, bidirectional antenna, 3-D printing, additively manufactured electronics (AME), 2-D beam scanning.**

I. INTRODUCTION

With the ever-increasing demand for communication capacity, millimeter-wave (mm-wave) bidirectional radiation antennas have attracted extensive attention since they have wide applications for microbase stations, railway and tunnel relay communications [1], [2]. To compensate for the atmospheric propagation loss of mm-waves, it needs high-gain bidirectional antennas with a pencil beam. For high-mobility mm-wave applications, to expand spatial coverage, the beam of a high-gain antenna should be steered within a wide frequency range [3], [4]. Thus, wideband bidirectional antennas with high gain and beam scanning capability are in demand.

Manuscript received May 1, 2023. This work was supported by the National Natural Science Foundation of China under Grant 61601026 and Grant 62071043.

Z. Zhai, F. Lin, and H. Sun are with School of Integrated Circuits and Electronics, Beijing Institute of Technology, Beijing 100081, China, and also with Beijing Key Laboratory of Millimeter Wave and Terahertz Technology. (E-mail: linfeng.scut@gmail.com, fenglin@bit.edu.cn).

Y. Yang is with School of Electrical and Data Engineering, University of Technology Sydney, Ultimo, NSW 2007, Australia (e-mail: yang.yang.au@ieee.org).

The conventional circuit-fed bidirectional antennas include SIW array antenna [1] and microstrip array antenna [5]-[7]. In [1], an mm-wave SIW bidirectional multibeam array antenna with 8×8 Butler matrices was realized. The measured gain is only 7.2–11.1 dBi, and the bandwidth is 28.6~31.2 GHz (8.7%). It needs a more complex feeding network for high-gain large-scale mm-wave array applications, resulting in high insertion loss, high fabrication cost and narrow bandwidth. As an alternative, spatially-fed transmit–reflect-array (TRA) antennas with bidirectional beams have aroused more interest since they feature lightweight, low-cost, high-efficiency feeding techniques and wide bandwidth [8]-[17]. The TRA antenna consists of reflectarray (RA) and transmitarray (TA) to generate the backward and forward pencil beams, respectively.

The first kind of TRA antennas [8], [9] only works in the simultaneous operating mode, generating backward and forward beams simultaneously. In [8], a TRA antenna using phase-shifting frequency-selection-surface (FSS) elements was proposed for the first time. The aperture efficiency is 15%, since it uses cross-polarized field components. The second kind of TRA antennas [10]-[15] can independently control backward and forward beams, working in simultaneous operating mode or time-division operating mode. In the time-division operating mode, the backward and forward beams are switched, which brings about a 3-dB gain improvement. In [11], a dual-band orthogonally-polarized TRA with a linearly-polarized feeder was proposed. The circularly polarized forward beam operates at 10 GHz with a 1-dB gain bandwidth of 14.2%, while the linearly polarized backward beam operates at 14 GHz with a 1-dB gain bandwidth of 10.4%. A slight difference exists between the gain bandwidths of backward and forward beams due to asymmetrical structure [9]-[15], causing a narrower overlapped bandwidth for bidirectional beams. In addition, in [8]-[15], there is a long distance between the feed source and the array, resulting in a relatively high profile of TRA antennas.

The aforementioned TRA antennas only achieve two fixed beams within a limited spatial coverage, which cannot satisfy the requirement of wide-beam coverage for mm-wave communication systems. Therefore, electronically scanning bidirectional spatially-fed array antennas were proposed by using PIN diodes [16], [17]. In [17], a reconfigurable bidirectional beam-steering aperture with TA, RA and TRA modes switching was proposed. However, they work in the low-frequency band (<11 GHz), and the aperture efficiencies are only 8.2% in [16] and 19.2% in [17], due to the loss of PIN diodes and quantization phase error of the array. Thus, it is

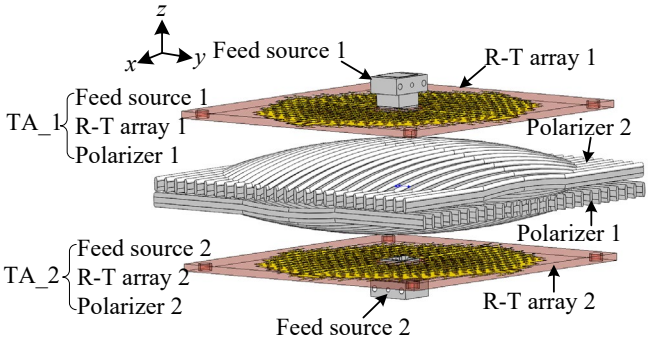

Fig. 1. Configuration of the proposed bidirectional antenna.

necessary to find new solutions for beam scanning for mm-wave bidirectional antennas with high aperture efficiency.

In this paper, an additively manufactured wideband low-profile bidirectional 2-D beam-scanning antenna is proposed for mm-wave applications. The backward and forward beams are independently controlled by two orthogonally mirrored folded TAs, which are composed of a feed source, a curved polarizer and an R-T array. The two folded TAs overlap in space to further reduce the antenna profile. A 3D-printed all-metal miniaturized ME dipole antenna is designed as a feed source integrated with the folded TA. The polarizer is realized by curved metal gratings for high-efficiency reflection. High isolation between two feed sources is obtained due to high cross-polarized ME dipoles and high polarization selective metal gratings. Based on the AME technique, the R-T array element is realized by two wideband tightly coupled bow-tie dipole antennas connected by a pair of differential microstrip-line phase shifters with true-time delay. The continuous 360° phase-shift tuning is obtained by changing the length of the microstrip-line phase shifters. Benefiting from the broadband characteristics of feed sources, polarizers and R-T array elements, a wide overlapped gain bandwidth for the backward and forward beams is obtained. Furthermore, the 2-D beam scanning capability with constant beam direction within a wide frequency is realized by moving the polarizer along the *x*- and *y*-directions. As a proof of concept, a 312-element antenna prototype working from 27 to 40 GHz is designed and experimentally characterized.

The rest of the paper is organized as follows. Section II presents the configuration, operating principle and design details of the proposed bidirectional antenna. Section III presents the simulation and measurements of the proposed bidirectional antenna. The conclusion is given in Section V.

II. Design of The Bidirectional Antenna Based on Double Folded Transmitarrays

A. Beam-Scanning Mechanism

Fig. 1 shows the configuration of the proposed bidirectional antenna, which consists of two orthogonally mirrored folded transmitarrays of TA_1 and TA_2. The folded TA_1 consists of R-T array 1, Polarizer 1 and Feed source 1, and the folded TA_2 consists of R-T array 2, Polarizer 2 and Feed source 2. The TA_1 and TA_2 are overlapped in space to reduce the total height of the antenna as much as possible. The R-T arrays 1 and

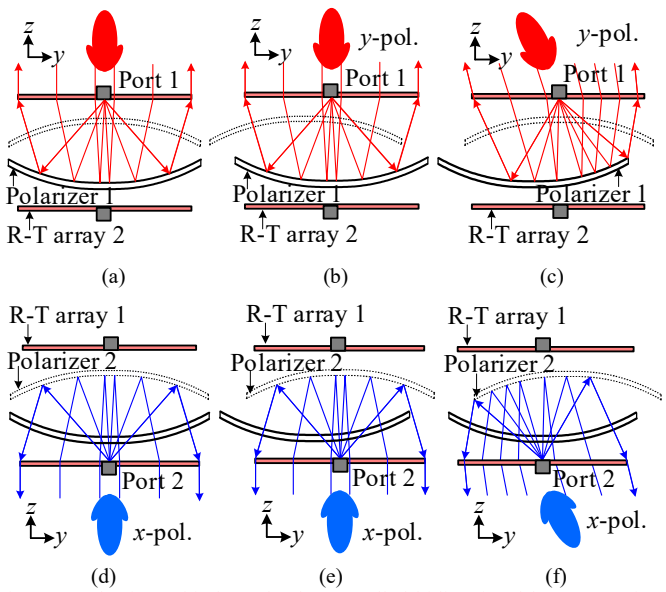

Fig. 2. Mechanism of independently controlled bidirectional beam scanning. (a) Port 1 excites. (b) Port 1 excites and polarizer 2 offsets. (c) Port 1 excites and polarizer 1 offsets. (d) Port 2 excites. (e) Port 2 excites and polarizer 1 offsets. (f) Port 2 excites and polarizer 2 offsets.

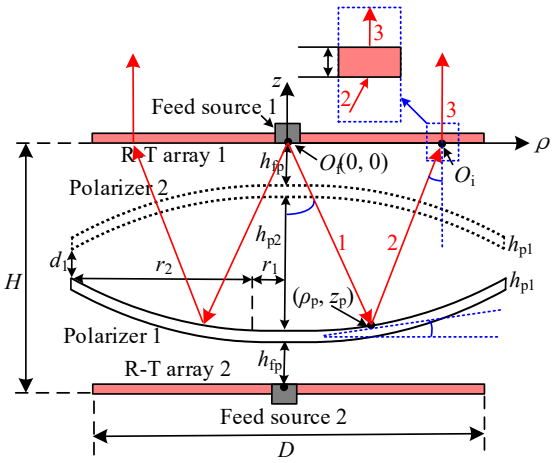

Fig. 3. Side-view of the proposed antenna for the 0° beam.

2 are located on the top and bottom, respectively. Polarizers 1 and 2 with curved surfaces are located between the R-T arrays 1 and 2. Feed sources 1 and 2 are located in the center of the R-T arrays 1 and 2, respectively. Feed source 1 and R-T array 1 work in *y*-direction linear polarization, while Feed source 2 and R-T array 2 work in *x*-direction linear polarization.

Fig. 2 shows the mechanism of independently controlled bidirectional beam scanning. The ports 1 and 2 represent the input ports of Feed sources 1 and 2, respectively. As shown in Fig. 2(a), when exciting the input port 1 of Feed source 1, the *y*-polarized incident wave (red line) is reflected by Polarizer 1, and arrives at R-T array 1. By utilizing the phase compensation of R-T array 1, TA_1 can generates *y*-polarized beams (in red color) in the +*z* direction. Polarizer 1 is designed to transmit *x*-polarized wave and reflect *y*-polarized wave, simultaneously, while Polarizer 2 is designed to transmit *y*-polarized wave and reflect *x*-polarized wave, simultaneously. In theory, the *y*-polarized incident waves radiated from Feed source 1 will

transmit Polarizer 2 and be entirely reflected by Polarizer 1. Thus, TA_2 (i.e., Polarizer 2, R-T array 2 and Feed source 2) does not affect the beam's characteristics in the $+z$ direction, and the beam direction will not change when Polarizer 2 moves, as shown in Fig. 2(b). The beam direction is determined by the position of Polarizer 1. Fig. 2(c) shows the beam direction changes to the left, with Polarizer 1 moving to the left. Similarly, when exciting the input port 2 of Feed source 2, an x-polarized beam is generated in the $-z$-direction, as shown in Fig. 2(d). TA_1 (i.e., Polarizer 1, R-T array 1 and Feed source 1) does not affect the beam's characteristics in the $+z$-direction, so the beam direction is not affected when Polarizer 1 moves, as shown in Fig. 2(e). Fig. 2(f) shows the beam direction changes to the right, with Polarizer 2 moving to the right. Thus, the bidirectional beam with independent scanning capability is realized.

Fig. 3 shows the side-view of the proposed antenna for the 0° beam. The diameters of the R-T arrays 1 and 2 are D. The height H between R-T arrays 1 and 2 equals $2h_{\mathrm{fp}}+2h_{\mathrm{p1}}+h_{\mathrm{p2}}$. h_{fp} is the distance between the Feed source 1 and Polarizer 2. h_{p1} and h_{p2} stand for the thickness of the Polarizers 1 and 2 and the distance between the apexes of Polarizers 1 and 2, respectively. d_1 is the distance between the ends of Polarizers 1 and 2. Under a cylindrical reference system (ρ, z), the upper surface of Polarizer 1 can be expressed as

$$\begin{cases} z_p = -H + h_{fp} + h_{p1} & 0 \le \rho_p < r_1 \\ (\rho_p - r_1)^2 + (z_p + H - h_{fp} - h_{p1} - R_s)^2 = R_s^2 & r_1 \le \rho_p \le r_1 + r_2 \end{cases} \tag{1}$$

For $0 \leqslant \rho_{\mathrm{p}} < r_1$, the surface of Polarizer 1 is a circular plane with a radius of r_1. For $r_1 < \rho_{\mathrm{p}} \leqslant r_2$, the Polarizer 1 is a spherical surface with a curvature radius of R_{s}. R_{s} is determined by

$$R_s = \frac{r_2^2 + (\frac{h_{p2}}{2} - \frac{d_1}{2})^2}{h_{p2} - d_1} . \tag{2}$$

The surfaces of Polarizers 1 and 2 are symmetrical along the plane of $z = -H/2$. The phase center of Feed source 1 is located at the point of $O_{\mathrm{f}}(0, 0)$, and Feed source 2 is located on $(-H, 0)$. The R-T arrays 1 and 2 are located on the plane $z = 0$ and $z = -H$, respectively.

Since the proposed antenna is symmetrical, the performances of the folded TAs 1 and 2 are the same. Without loss of generality, the working mechanism of folded TA 1 is analyzed by using the folded ray-tracing principle [18]-[20]. As shown in Fig. 3, the incident wave (ray 1) radiated from Feed source 1 is reflected by Polarizer 1. Then, the reflected wave (ray 2) arrives at the location O_{i} (ρ_{i} 0) (i.e., element i) of the R-T array 1. The incident angles of α and β are calculated by (3) and (4), respectively.

$$\alpha = \arctan\frac{\rho_{\mathrm{p}}}{z_p} = \begin{cases} \arctan\dfrac{\rho_p}{H - h_{fp} - h_{p1}} & 0 \le \rho_p < r_1 \\ \arctan\dfrac{\rho_p}{-\sqrt{R_s^2 - (\rho_p - r_1)^2} + R_s + h_{fp} + h_{p1} - H} & r_1 \le \rho_p \le r_1 + r_2 \end{cases} \tag{3}$$

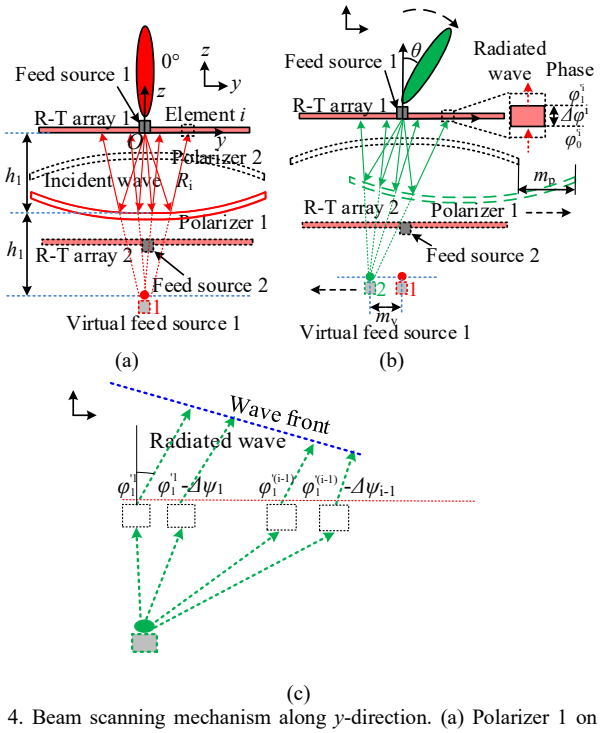

Fig. 4. Beam scanning mechanism along y-direction. (a) Polarizer 1 on the center. (b) Polarizer 1 moving along y-axis (offset the center). (c) Phase distributions for the R-T array 1.

$$\beta = \alpha - 2\theta \tag{4}$$

$$\theta = \arctan\frac{dz_p}{d\rho_p} = \begin{cases} 0 & 0 \le \rho_p < r_1 \\ \arctan\dfrac{\rho_p - r_1}{\sqrt{R_s^2 - (\rho_p - r_1)^2}} & r_1 \le \rho_p \le r_1 + r_2 \end{cases} \tag{5}$$

θ is the angle between the tangent of Polarizer 1 and ρ-axis. From Fig. 3, the following relationship can be obtained.

$$\rho_i = \rho_p - z_p \tan\beta \tag{6}$$

For the 0° beam (see Fig. 3), the incident wave phase φ_0^{i} of element i can be expressed as

$$\varphi_0^i = -\frac{2\pi f}{c}(P_i^1 + P_i^2) = -\frac{2\pi f}{c}\left(\sqrt{z_p^2} + \sqrt{z_p^2 + (\rho_p - \rho_i)^2}\right) \tag{7}$$

where P_{i}^1 and P_{i}^2 are the path length of ray 1 and ray 2, respectively. c and f are the velocity of the free space wave and operating frequency, respectively. The phase shift of element i is $\Delta\varphi_{\mathrm{i}}$. To realize a high gain beam at 0°, the radiated wave phase φ_1^{i} of element i should be independent with i. Based on (7), the radiated wave phase φ_1^{i} of element i ($=\varphi_0^i + \Delta\varphi^i$) can be calculated as

$$\varphi_1^i = \varphi_0^i + \Delta\varphi^i = -\frac{2\pi f}{c}(P_i^1 + P_i^2 - \frac{c}{2\pi f}\Delta\varphi_i) = -\frac{2\pi f}{c}L_{cons\tan t} \tag{8}$$

where L_{constant} is a distance constant. Thus, from (8), the $\Delta\varphi_{\mathrm{i}}$ for the 0° beam can be calculated as

$$\Delta\varphi_i = \frac{2\pi f}{c}(P_i^1 + P_i^2 - L_{cons\tan t}) . \tag{9}$$

Fig. 4 shows the beam scanning mechanism along y-direction. Based on the methods in [18]-[20], the beam scanning mechanism of the folded TA can be analyzed by using the virtual feed source. As shown in Fig. 4(a), When Polarizer 1 is

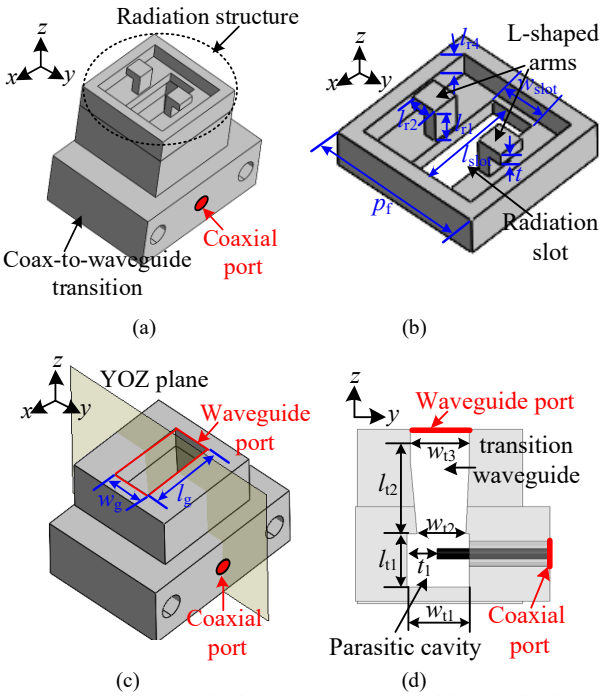

Fig. 5. Configuration of the feed source. (a) 3D view of the ME dipole antenna. (b) 3D view of the radiation structure. (c) 3D view of the coax-to-waveguide transition. (d) *YOZ* plane of the coax-to-waveguide transition.

on the center, it can be regarded as the Virtual feed source 1 is on the center. The distance between Virtual feed source 1 and Feed source 1 equals to $2h_1$, where h_1 is the distance between the apexes of Polarizer 1 and R-T array 1. The path length R_i between Virtual feed source 1 and element i equals to $P_i^1+P_i^2$. As shown in Fig. 4(b), when the Polarizer 1 moves from the center to the right by m_p, it can be regarded as the Virtual feed source 1 moves from the center to the left by m_v. then, the path length changes to $R_i^{'}$. The incident wave phase $\varphi_0^{'i}$ of element i can be expressed as

$$\varphi_0^{'i} = -\frac{2\pi f}{c} R_i^{'} \tag{10}$$

Based on (9) and (10), the radiated wave phase $\varphi_1^{'i}$ of element i ($=\varphi_0^{'i}+\Delta\varphi^i$) can be calculated as

$$\varphi_1^{'i} = \varphi_0^{'i} + \Delta\varphi^i = -\frac{2\pi f}{c}(R_i^{'} - P_i^1 - P_i^2 - L_{cons\tan t}) . \tag{11}$$

When the value i increases, the wave phasefront $\varphi_1^{'i}$ decreases, which results in a gradient phase distribution along the y-direction. Due to the gradient phase distribution, as shown in Fig. 4(c), the antenna generates the θ beam along y-direction, which is similar to other mechanically scanning transmitarray [21], [22]. Similarly, beam scanning in the x-direction can be realized by moving Polarizer 1 along the x-axis.

Based on (11), the corresponding time delay $T_1^{'i}$ of the radiated wave of element i can be calculated as

$$T_1^{'i} = \frac{\varphi_1^{'i}}{2\pi f} = -\frac{R_i^{'} - P_i^1 - P_i^2 - L_{cons\tan t}}{c} \tag{12}$$

From (12), the time delay $T_1^{'i}$ is frequency independent, which indicates the constant beam direction is realized for the θ beam.

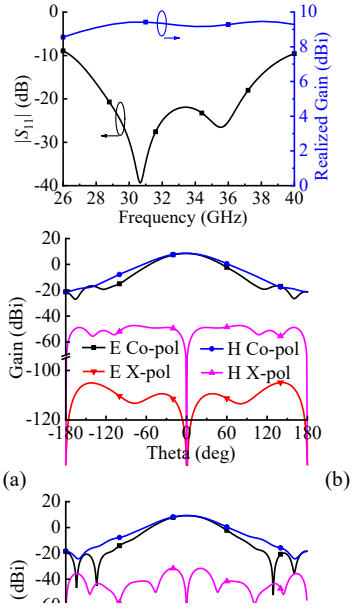

B. *Feed Source*

Fig. 5 shows the configuration of the proposed feed source. It adopts an all-metal ME dipole antenna, which features high gain, small size, wide gain bandwidth and stable pattern. Fig. 5(a) shows the ME dipole antenna consists of a radiation structure and a coax-to-waveguide transition. The radiation structure comprises a radiation slot and a pair of L-shaped metallic arms, as shown in Fig. 5(b). Two L-shaped arms are placed at the center of the slot edge and work as an electric dipole in the y-direction. The radiation slot can be equivalent to a magnetic dipole in the x-direction. Two resonance modes are generated by the electric and magnetic dipoles [23]-[24]. To excite the electric and magnetic dipoles simultaneously, a wideband coax-to-waveguide transition is designed, with reference to [25], as shown in Fig. 5(c). The transition consists of a coaxial probe, a parasitic cavity and a transition waveguide, as shown in Fig. 4(d). By tuning the parameters of t_1, w_{t1}, w_{t2} and l_{t2}, the wideband impedance matching can be achieved.

Fig. 6 shows the simulated results of the proposed ME dipole antenna with final dimensions of l_{r1} = 1.7, l_{r2} = 1.7, l_{r3} = 8, l_{r4} =1.5, l_{slot} = 7.11, w_{slot} = 2.9, t = 0.8, p_f = 10, l_{t1} = 3.2, l_{t2} = 4.3, w_{t1} = 3.76, w_{t2} = 2.96, w_{t3} = 3.56, t_1 = 1.68, w_g = 3.56, l_g = 7.11 (unit: mm). Fig. 6(a) shows the 10-dB matching bandwidth and 1-dB gain bandwidth are 40.2% and 42.4%, respectively. The simulated realized gain of feed source ranges from 8.6 to 9.5 dBi within 26 to 40 GHz. Fig. 6(c)-(e) show the radiation patterns at 26, 33 and 40 GHz, respectively. The cross-polarization levels are lower than -60 dB in the broadside direction with the front-to-back ratio of higher than 28 dB.

C. *Polarizer*

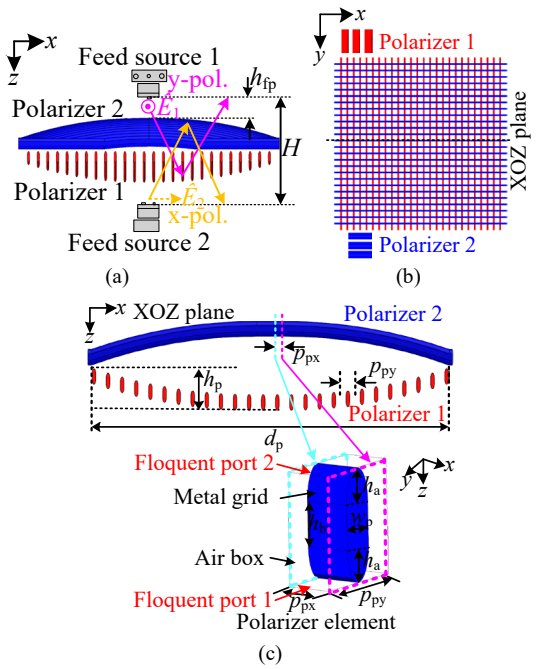

Fig. 7. Configuration of the curved polarizers. (a) 3D view. (b) Top view. (c) *XOZ* plane and polarizer element.

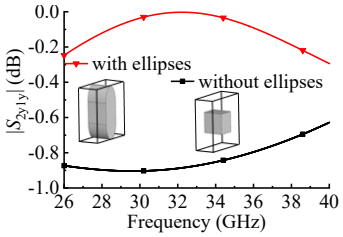

Fig. 8. Simulated transmission coefficients of the polarizer element with and without semi-ellipses in *y*-polarization.

As mentioned above, Polarizer 1 needs to transmit *x*-polarized wave and reflect *y*-polarized wave. In addition, Polarizer 1 should provide phase tuning for *y*-polarized reflected waves. To realize phase tuning for reflected waves, traditional planar reflectarrays usually consist of multilayer structures with phase-shift elements. For the purpose of simple structure and easy integration, a spherical polarizer is used in this design, since it doesn't need additional phase-shift structure. Fig. 7(a) shows the configuration of the proposed curved polarizers, which consist of two same Polarizers 1 and 2. As shown in Fig. 7(b), Polarizer 1 is rotated by 90° with respect to Polarizer 2, and Polarizer 1 consists of a series of parallel curved metal gratings with the same distance of p_{py}. The co-polarization direction (i.e., *y*-polarization) of Feed source 1 is parallel with the metal gratings direction of Polarizer 1, which is perpendicular to the metal gratings direction of Polarizer 2. The co-polarization direction (i.e., *x*-polarization) of Feed source 2 is parallel to the metal gratings direction of Polarizer 2, which is perpendicular to the metal gratings direction of Polarizer 1. When exciting Feed source 1 with the *y*-polarized wave, the two adjacent metal gratings of Polarizer 2 work as a parallel-plate waveguide. Therefore, the *y*-polarized wave can pass through Polarizer 2. While the *y*-polarized EM

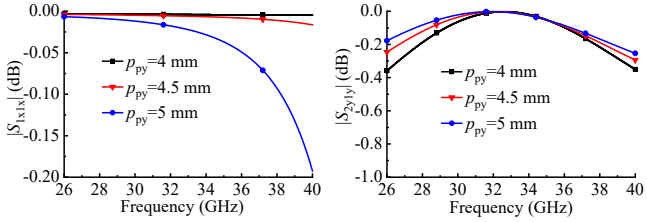

Fig. 9. Simulated *S*-parameter of the polarizer element with different p_{px}. (a) *x*-polarized reflection coefficient S_{1x1x}. (b) *y*-polarized transmission coefficient S_{2y1y}.

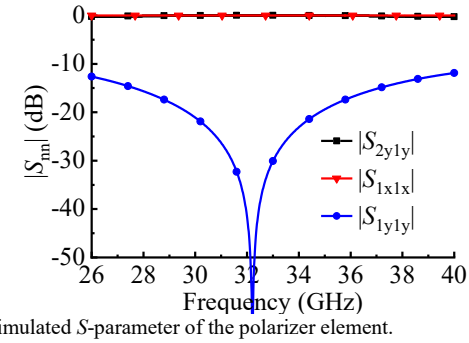

Fig. 10. Simulated *S*-parameter of the polarizer element.

wave is reflected by Polarizer 1, since it is parallel to the metal gratings of Polarizer 1. Similarly, when exciting the port 2 with the *x*-polarized wave, the *x*-polarized wave will pass through Polarizer 1 and be reflected by Polarizer 2. Thus, Polarizer 2 reflects the *x*-polarized wave and transmits the *y*-polarized wave. To obtain high aperture efficiency and wide gain bandwidth, the height h_p of Polarizer 2 (see Fig. 7(c)) should be as large as possible [20]. The distance h_{fp} between Polarizer 2 and Feed source 1 is optimized to realize good port matching of feed sources and low antenna profile. To obtain a large coverage for incident waves when Polarizer 1 moves, the diameter d_p of Polarizer 1 is slightly larger than that of the R-T array.

To estimate the transmission and reflection efficiencies of Polarizers 1 and 2, the polarizer element with two floquent ports and an air box is simulated under periodic boundary conditions, as shown in Fig. 7(c). The cross-section of the polarizer element consists of a rectangle with a length of h_b and a width of w_p, connected by two semi-ellipses with a long axis of h_a and a short axis of w_p on its ends. The semi-ellipse metal structure acts as a transition between the free space and parallel-plate waveguide to improve the transmission efficiency of the polarizer. Fig. 8 shows that the *y*-polarized transmission coefficient $|S_{2y1y}|$ is increased by more than 0.8 dB at 33 GHz with the semi-ellipse structures.

Fig. 9(a) shows the *x*-polarized reflection coefficient $|S_{1x1x}|$ decreases with the increasing p_{py} between metal gratings. Fig. 9(b) shows the *y*-polarized transmission coefficient $|S_{2y1y}|$ increases with the rising p_{py}. Fig. 10 shows the simulated *S*-parameters of the polarizer element with final dimensions of $p_{py} = 4.5$, $w_p = 1.6$, $h_a = 1.5$, $h_b = 2$ (unit: mm). The transmission coefficient $|S_{2y1y}|$ and reflection coefficient $|S_{1x1x}|$ are nearly 0 dB within the 26 ~ 40 GHz frequency range. The reflection coefficient $|S_{1y1y}|$ is less than -10 dB from 26 to 40 GHz.

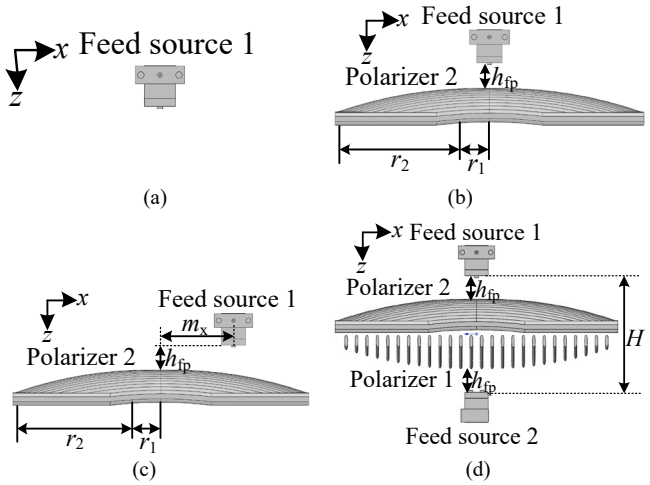

Fig. 11. Different combinations of feed sources and polarizers. (a) Feed source 1. (b) Feed source 1 and Polarizer 2. (c) Feed source 1 and offset Polarizer 2. (d) Feed sources 1, 2 and offset Polarizers 1, 2.

To estimate the performances of Polarizers 1 and 2, four combinations of feed sources and polarizers are simulated, as shown in Fig. 11. In Fig. 11(a), there is only Feed source 1. Fig. 11(b) and (c) show Feed source 1 with Polarizer 2 and with offset Polarizer 2, respectively. Fig. 11(d) contains orthogonally mirrored Feed sources 1 and 2 along with Polarizers 1 and 2. Fig. 12 shows the simulated *S*-parameters and realized gains of the four cases with final dimensions of H = 49.5, h_{fp} = 10, m_x = 15, r_1 = 5, r_2 = 55 (unit: mm). Fig. 13 shows the simulated radiation patterns of Feed source 1 with and without Polarizer 2 at 33 GHz. As shown in Fig. 12, with Polarizer 2 or offset Polarizer 2, the $|S_{11}|$ and realized gains of Feed source 1 have small variations. Fig. 13 shows that with Polarizer 2 or offset Polarizer 2, the E-plane and H-plane patterns of Feed source 1 almost keep the same within ±60° region. Thus, Polarizer 2 achieves good transmission efficiency for the *x*-polarized wave. Fig. 12 shows the isolation between Feed sources 1 and 2 is better than 100 dB within 26 ~ 40 GHz.

D. R-T Array Element

Fig. 14 shows the configuration of the proposed R-T array element with two tightly coupled bow-tie dipole antenna. From (9), the phase-shift of R-T array element $\Delta\varphi_i$ should be linear with frequency to realize a correctly compensated phase within a wide bandwidth. As shown in Fig. 14(a), two wideband tightly coupled bow-tie dipole antennas act as the receiving and transmitting antennas, which are symmetrical about the ground. The incident and transmitted waves are both linear polarizations in the *x*-axis direction. Two pairs of differential microstrip lines with a length of l_m (see Fig. 14(b)) work as a true-time-delay phase shifter to transfer the energy from the receiving antenna to the transmitting antenna with the required phase and low loss. The metal holes connect the parts of microstrip lines above and below the ground with a height of h_{t1}. The differential microstrip lines are connected to the receiving and transmitting antennas by the metal holes with a height of h_{t2}, as shown in Fig. 14(b). To realize the required phase modulation, the phase shift between the receiving and transmitting antennas should be continuous 360° coverage. The continuous phase tuning of 360°

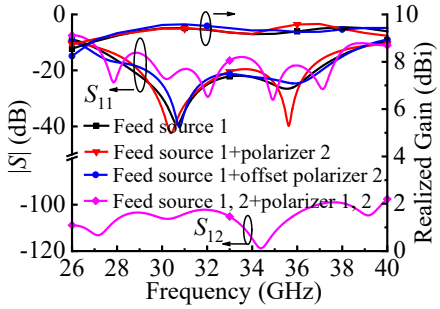

Fig. 12. Simulated *S*-parameter and realized gain for different combinations of feed sources and polarizers.

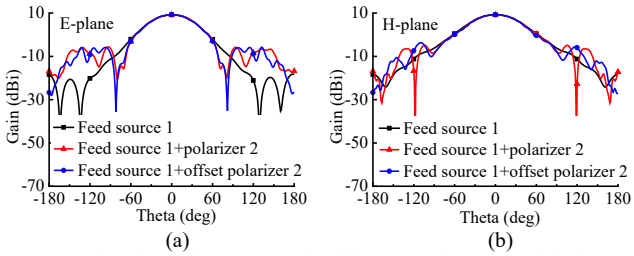

Fig. 13. Simulated radiation patterns for different combinations of feed sources and polarizers at 33GHz. (a) E-plane. (b) H-plane.

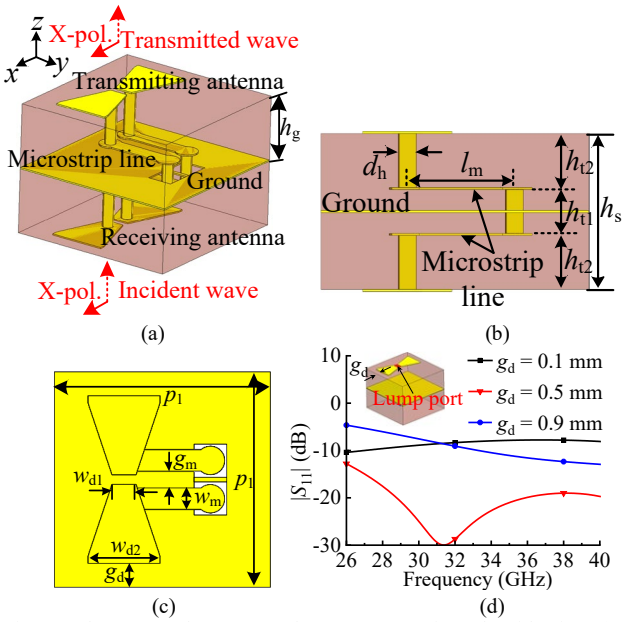

Fig. 14. The proposed R-T array element. (a) 3D view. (b) Side view. (c) Top view. (d) Simulated reflection coefficient of transmitting antenna.

is realized by changing the length $2l_m$ of the differential microstrip lines.

As shown in Fig. 14(c), to avoid grating lobes of the array, the element size p_1 is set to 4.5 mm (~0.4 λ_L, λ_L is the wavelength at the lowest working frequency of 27 GHz). The impedance bandwidth of the tightly coupled bow-tie dipole antenna is affected by the mutual capacitance between adjacent antenna elements and the inductance caused by the ground [26]-[28]. The mutual capacitance is determined by the width w_{d2} of the bow-tie and the distance g_d. The inductance coming from ground is determined by the distance h_g between the bow-tie and the ground. By properly adjusting the values of w_{d2},

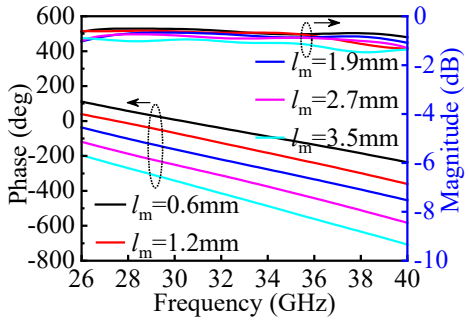

Fig. 15. Simulated transmission responses under normal incidence.

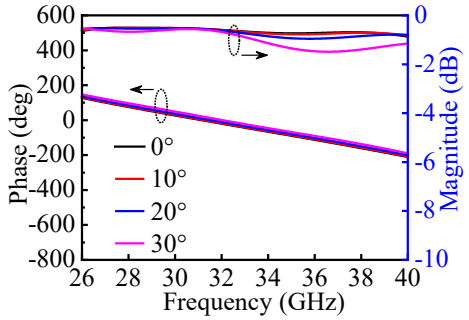

Fig. 16. Simulated transmission responses under different oblique incidence angles.

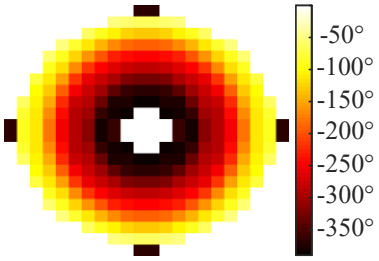

Fig. 17. Required phase distributions on the aperture of the R-T array.

g_d and h_g, the mutual capacitance can cancel out the inductance coming from the ground, resulting in a wide impedance bandwidth. The h_g is set as 1.2 mm ($0.1\lambda_L$). Fig. 14(d) shows the simulated reflection coefficient of the transmitting antenna when the distance g_d changes from 0.1 mm to 0.9 mm. The impedance of the lumped port is set to 150 Ω. When the distance g_d is 0.5 mm, the optimized 10-dB matching bandwidth is realized from 26 to 40 GHz (42.4%). Therefore, by properly adjusting g_d, one can control the mutual coupling between adjacent antenna elements and obtain optimal matching bandwidth.

The proposed R-T array element is realized by the AME technique, which can 3D print the conductive and dielectric materials, simultaneously [29]-[31]. The printed dielectric material is ultraviolet (UV) curable acrylate ink with a dielectric constant 2.8 and a loss tangent 0.013 [29]. All the conductor layers are printed using silver nanoparticle ink with a thickness of 35 μm. All the diameters d_h of the metal holes are 0.3 mm. Thanks to the AME technique, the element thickness h_s and interlayer distances h_{t1}, h_{t2} can be kindly adjusted, which improves the design flexibility.

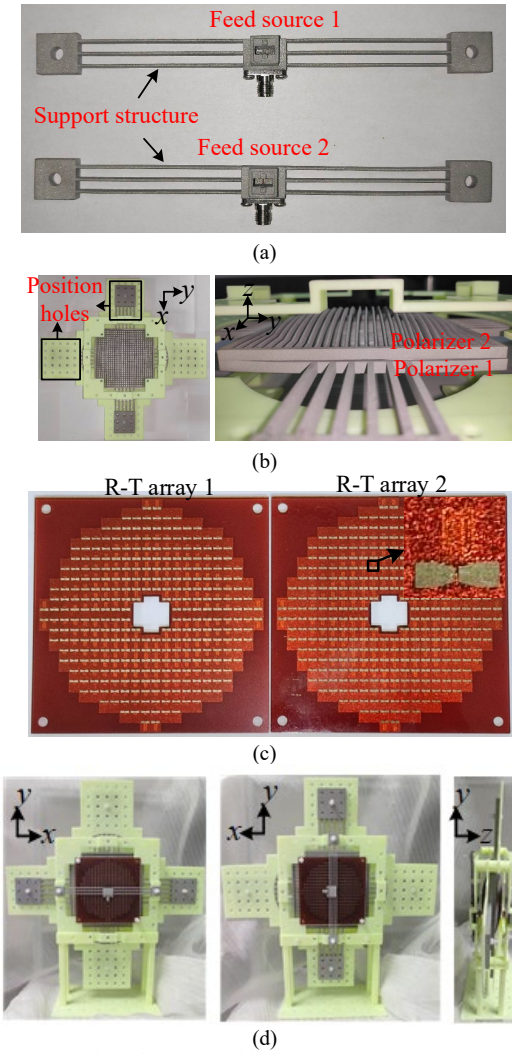

Fig. 18. Photograph of the proposed bidirectional antenna. (a) Feed sources 1 and 2. (b) Polarizers 1 and 2. (c) R-T arrays 1 and 2. (d) Total structure.

A full-wave simulation is conducted for the R-T array element with final optimal dimensions of $p_1 = 4.5$, $w_{d1} = 0.5$, $w_{d2} = 1.1$, $g_d = 0.9$, $w_m = 0.45$, $g_m = 0.35$, $h_{t1} = 0.32$, $h_{t2} = 1.04$, $h_s = 2.4$, $d_h = 0.3$(unit: mm). When a normal incidence plane-wave is applied, the simulated transmission responses with different lengths l_m of the microstrip lines are shown in Fig. 15. When l_m changes from 0.6 to 3.5 mm, the amplitudes of transmission coefficients are greater than -1.4 dB from 26 to 40 GHz. The phases are almost linear as a function of frequency. By tuning the l_m from 0.6 mm to 3.5 mm, the phase-shift tuning range of the proposed element is larger than 360° at 33 GHz. Fig. 16 shows the simulated transmission responses under different oblique incidence angles. The phase deviation within oblique incident angle range of 30° is less than 20° from 26 GHz to 40 GHz. The insertion losses for all states from 26 GHz to 40 GHz are less than 1.5 dB.

E. Results of Simulation and Measurement

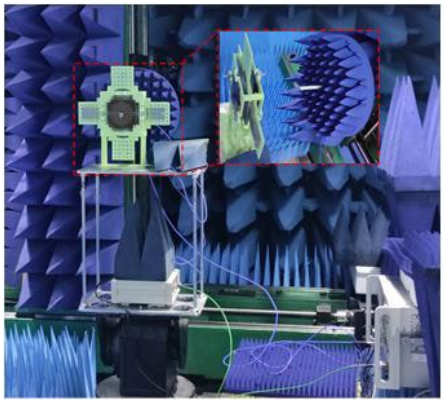

Fig. 19. Proposed bidirectional antenna in the near-field anechoic chamber.

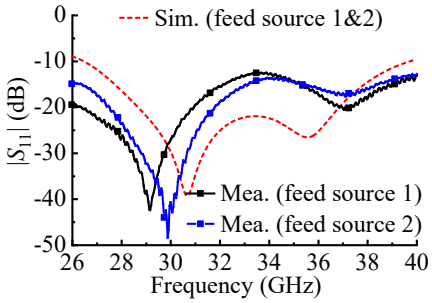

Fig. 20. Reflection coefficient of the feed sources.

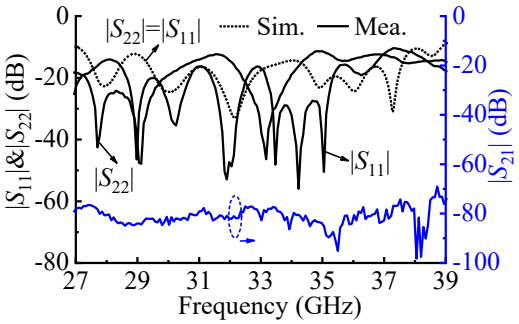

Fig. 21. Simulated and measured *S*-parameters of the bidirectional antenna.

For verification, a bidirectional antenna with 312-element R-T arrays working from 27 GHz to 40 GHz is designed and simulated. Fig. 17 shows the required phase compensation distribution on the aperture of the R-T array at 33 GHz, which was calculated by (1)-(6), (9). Fig. 18 shows the photo of the fabricated bidirectional antenna with final dimensions of $D = 99$, $H = 49.5$, $h_{fp} = 9.75$, $h_{p1} = 5$, $h_{p2} = 20$, $r_1 = 5$, $r_2 = 55$, $d_1 = 1$ (unit: mm). As shown in Fig. 18(a), Feed sources 1 and 2 with support structures are printed by metal 3D printing technique. The support structure consists of three metal gratings. As shown in Fig. 18(b), Polarizers 1 and 2 are also printed by metal 3D printing technique. To realize the 2-D beam scanning capability, Polarizers 1 and 2 are independently moved along the *x*- and *y*-direction, respectively. As shown in Fig. 18(c), the 312-element R-T arrays are fabricated by AME technique [29]-[31]. The printing resolutions are 18 μm, 18 μm and 10 μm in the *x*-, *y*- and *z*-direction, respectively. The printing time of a 312-element R-T array is about 4 hours. To integrate the feed source in the center of the R-T array, the center 12 elements are taken out. The feed sources, polarizers and R-T arrays are fixed

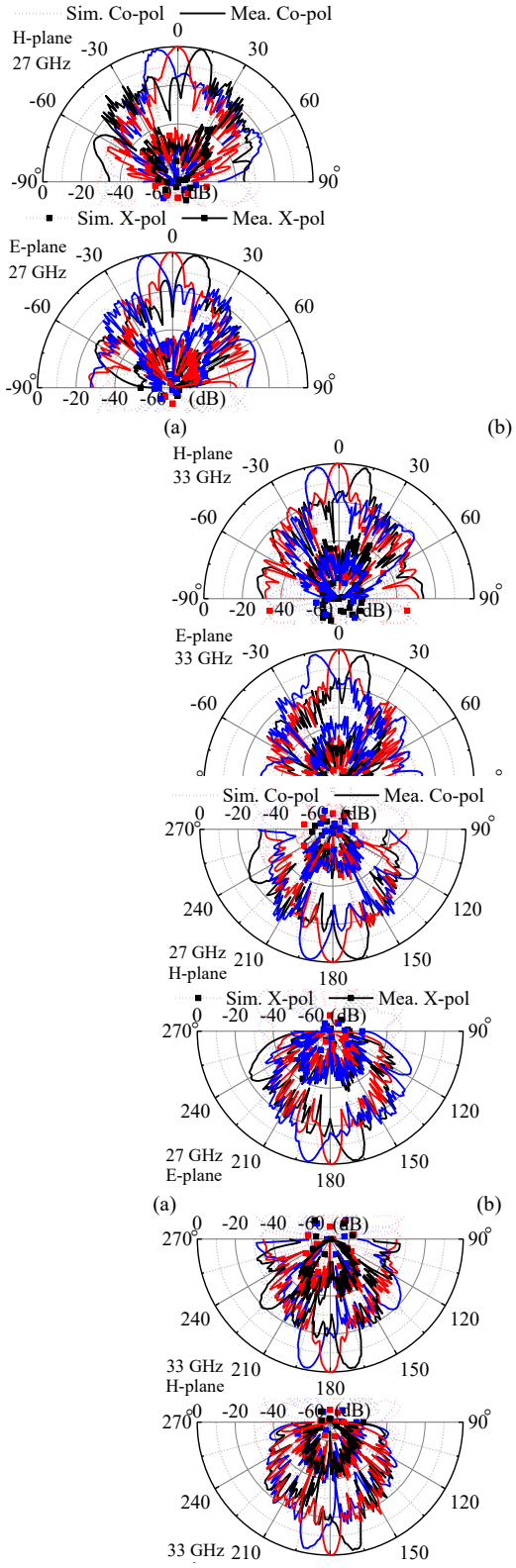

by Nylon screws, and the total structure is shown in Fig. 18(d). As shown in Fig. 19, the bidirectional antenna was measured in a near-field anechoic chamber.

Fig. 20 shows the measured 10-dB bandwidth of feed sources is 42.4% (26~40 GHz). Fig. 21 shows the measured 10-dB bandwidth of the bidirectional antenna is 36.4% (27~39 GHz) with measured isolation of better than 70 dB. Fig. 22 shows the simulated and measured normalized patterns in the forward

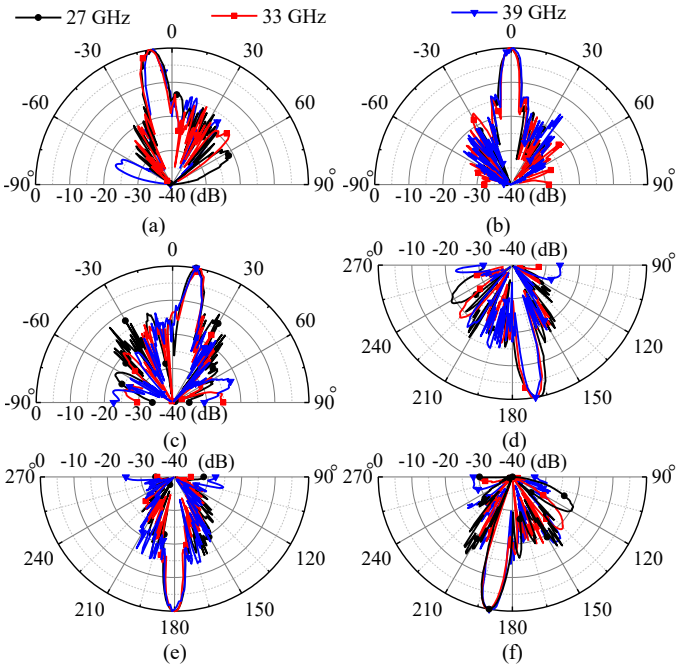

Fig. 24. Measured normalized H-plane patterns versus frequency. (a) -10°. (b) 0°. (c) 10°. (d) 170°. (e) 180°. (f) 190°.

direction at 27, 33, and 39 GHz. When Polarizer 1 is located in the center, the measured beam directs to 0°. When Polarizer 1 moves from the center along the *x*-axis and *y*-axis by ±30 mm, the measured beams direct to ±10° in the H-plane and E-plane, respectively. Fig. 23 shows the simulated and measured normalized patterns in the backward direction at 27, 33, and 39 GHz. When Polarizer 2 is located in the center, the measured beam directs to 180°.When Polarizer 2 moves from the center along the *x*-axis and *y*-axis by ±30 mm, the measured beams direct to 170° and 190° in the E-plane and H-plane, respectively. In the broadside directions of 0° and 180°, the measured sidelobe levels are better than -15 dB, and the measured cross-polarization levels are below -40 dB. For all scanning

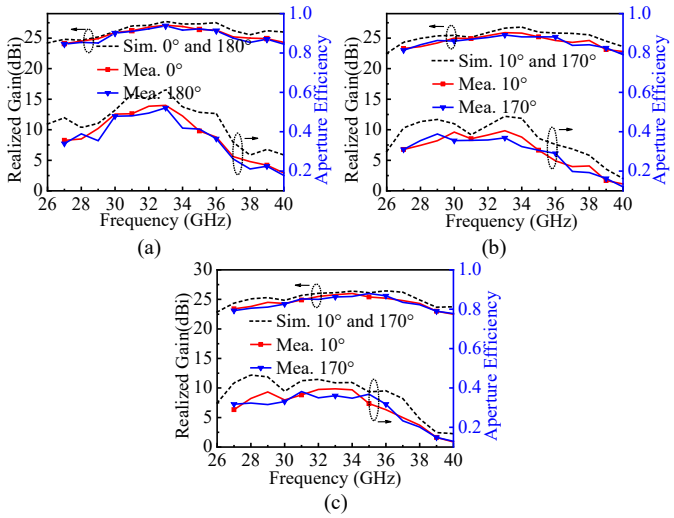

Fig. 25. Simulated and measured realized gains and aperture efficiencies of the bidirectional antenna. (a) 0° and 180°. (b) 10° and 170° in H-plane. (c) 10° and 170° in E-plane.

states, the measured sidelobe levels are better than -13 dB, and the measured cross-polarization levels are below -35 dB. Fig. 22 and 23 show that the bidirectional antenna can perform 2-D beam scanning within 27~39 GHz by moving polarizers along the *x*- and *y*-directions. To further illustrate the beam scanning with constant beam direction, Fig. 24 (a)~(f) shows the measured normalized H-plane patterns versus frequency for beams of -10°, 0°, 10°, 170°, 180° and 190°, respectivly. As shown, for all scanning states, the measured maximum pointing errors are less than 1° from 27 to 39 GHz.

Fig. 25 shows the simulated and measured realized gains and aperture efficiencies in different directions. As shown in Fig. 25(a), the simulated maximum gain for 0° and 180° beams is 27.7 dBi at 33 GHz. The simulated peak aperture efficiency for 0° and 180° beams is 61.3% at 33 GHz. The simulated 1-dB and 3-dB overlapped gain bandwidths for 0° and 180° beams are 16.5% (30.5~36 GHz) and 39.5% (26.8~40 GHz), respectively. The measured maximum gains for 0° and 180° beams are 27.1

TABLE I

COMPARISONS WITH OTHER REPORTED SPATIALLY-FED ARRAY ANTENNAS

	Freq (GHz)	Type	Peak Gain 0°/180° (dBi)	Peak aperture efficiency 0°/180°	*H*/*D*	Gain bandwidth in 0°/180°/overlapped	Bidirectional independent scanning	Scanning type
[8]	10	TA+RA	25.5 / 25	15% / 14%	1	15% / 14% / 14% (1-dB) 20% / 20% / 20% (3-dB)	No	N.A
[9]	30	TA+RA	21.4 / 24.4	7% / 14%	0.72	6.7% / 9.3% / 6.7% (1-dB)	No	N.A
[12]	9.4	TA+RA	20.3 / 20.3	45.5% / 41.8%	0.7	7.4% / 5.2% / 5.2% (1-dB)	No	N.A
[13]	10	TA+RA	21.1 / 21.2	29.5% / 29.6%	0.71	12.5% / 21% / 12.5% (1-dB) 20.8% / 27.5% / 20.8% (3-dB)	No	N.A
[16]	5.35	TA+RA	17.2 / 15.4	8.2% / 5.4%	1	19% / 22% / 19% (1-dB) 32% / 32% / 32% (3-dB)	No	2D Electrical scanning
[17]	9.5	TA+RA	21.4 / 21	19.2% / 17.3%	N.A	19.5% / 19.9% / 19.5% (3-dB)	Yes	2D Electrical scanning
[22]	27	TA	18.5	24.8%	0.44	33.3% (3-dB)	No	1D Mechanical scanning
[32]	28.5	TA	19.8	15.9%	0.67	16.2% (3-dB)	No	2D Electrical scanning
[33]	12.8	TA	18.4	20.2%	0.74	9.4% (3-dB)	No	2D Electrical scanning
This work	**33**	**TA+TA**	**27.1 / 27.0**	**53.4% / 52.2%**	**0.5**	**18.7% / 18.7% / 18.7% (1-dB) 38.8% / 38.8% / 38.8% (3-dB)**	**Yes**	**2D Mechanical scanning**

dBi and 27 dBi, respectively. The measured peak aperture efficiencies for 0° and 180° beams are 53.4% and 52.2%, respectively. The 1-dB and 3-dB overlapped gain bandwidths for 0° and 180° beams are 18.7% (30~36.2 GHz) and 38.8% (27 ~ 40 GHz), respectively. As shown in Fig. 25(b), the measured maximum gains for 10° and 170° beams in H-plane are 25.9 dBi and 25.5 dBi, respectively. The measured peak aperture efficiencies for 10° and 170° beams in H-plane are 40.5% and 36.9%, respectively. The measured 1-dB and 3-dB overlapped gain bandwidths for 10° and 170° beams in H-plane are 16.7% (30~35.5 GHz) and 38.8% (27~40 GHz), respectively. As shown in Fig. 25(c), the measured maximum gains for 10° and 170° beams in the E-plane are both 26 dBi. The measured peak aperture efficiencies for 10° and 170° beams in the E-plane are 38.2% and 39.6%, respectively. The measured 1-dB and 3-dB overlapped gain bandwidths for 10° and 170° beams in E-plane are 14.9% (31~36 GHz) and 36.3% (27~39 GHz), respectively. The measured scanning losses are below 1.7 dB and 1.9 dB in the H-plane and E-plane within 27~40 GHz, respectively.

Table I compares the measured performances of this work with the previously reported spatially-fed array antennas. Compared with other state-of-the-art works [8], [9], [12]-[17], the proposed antenna has the highest efficiency, lowest height-to-diameter ratio (*H*/*D*) and widest gain bandwidths at directions of 0° and 180°. In addition, only the bidirectional antenna in [17] and this work show bidirectional independent 2-D beam-scanning capability. Compared with [17], the proposed antenna exhibits better aperture efficiency. The antennas in [22], [32] and [33] exhibit unidirectional beam scanning, while the proposed antenna achieves bidirectional beam scanning. In addition, compared with antennas in [22], [32] and [33], the proposed antenna shows higher aperture efficiency and wider 3-dB gain bandwidth.

III. Conclusion

A wideband low-profile bidirectional 2-D beam-scanning antenna was proposed. Two orthogonally mirrored folded TAs overlapping in space achieved independent bidirectional beams and reduced antenna profile. The folded TA consists of a wideband feed source of ME dipole antenna, an efficient polarizer with curved metal gratings and a wideband R-T array with true-time delay. A 312-element antenna operating from 27 to 40 GHz was fabricated and measured for verification. Wide 1-dB gain bandwidth (18.7%), high aperture efficiency (53.4%) and low profile (*H/D* is 0.5) were achieved. The 2-D bidirectional beam-scanning coverage of ±10° with a maximum scanning loss of 1.9 dB was realized. The proposed bidirectional antenna can be a good candidate for modern millimeter-wave wireless communication systems, such as tunnel relay communications and microbase stations.

References

[1] Q. Sun, Y. L. Ban, J. W. Lian, Y. Yang, G. Wu and Y. X. Che, "Planar dual-polarization bidirectional multibeam array antenna for millimeter-wave applications," *IEEE Trans. Antennas Propag*., vol. 69, no. 10, pp. 6420-6430, Oct. 2021.

[2] G. Dong, Y. Liu, X. Li and A. Zhang, "Ultrawideband spoof surface plasmon polariton bidirectional endfire antenna based on wave vectors mismatching," *IEEE Trans. Antennas Propag*., vol. 69, no. 11, pp. 7895-7899, Nov. 2021.

[3] A. A. Baba, R. M. Hashmi, K. P. Esselle, M. Attygalle and D. Borg, "A millimeter-wave antenna system for wideband 2-D beam steering," *IEEE Trans. Antennas Propag*., vol. 68, no. 5, pp. 3453-3464, May. 2020.

[4] W. Hong *et al*., "Multibeam antenna technologies for 5G wireless communications," *IEEE Trans. Antennas Propag*., vol. 65, no. 12, pp. 6231-6249, Dec. 2017.

[5] H. Iwasaki, "A back-to-back rectangular-patch antenna fed by a CPW," *IEEE Trans. Antennas Propag.*, vol. 46, no. 10, pp. 1527–1530, Oct. 1998.

[6] J.-C.-S. Chieh and A.-V. Pham, "A bidirectional microstrip X-band antenna array on liquid crystal polymer for beamforming applications," *IEEE Trans. Antennas Propag*., vol. 61, no. 6, pp. 3364-3368, June. 2013.

[7] J. Wu, R. Lian, Z. Wang, and Y. Yin, **"** Strip-coupling circularly polarized antenna and its same-sense bidirectional array," *J. Electromagn. Waves Appl.*, vol. 29, no. 14, pp. 1859–1866, Sep. 2015.

[8] F. Yang, R. Deng, S. Xu, and M. Li, "Design and experiment of a near-zero-thickness high-gain transmit-reflect-array antenna using anisotropic metasurface," *IEEE Trans. Antennas Propag*., vol. 66, no. 6, pp. 2853–2861, Jun. 2018.

[9] S. L. Liu, X. Q. Lin, Y. H. Yan and Y. L. Fan, "Generation of a high-gain bidirectional transmit–reflect-array antenna with asymmetric beams using sparse-array method," *IEEE Trans. Antennas Propag*., vol. 69, no. 6, pp. 6087-6092, Sept. 2021.

[10] S. Liu and Q. Chen, "A wideband, multifunctional reflect-transmit-array antenna with polarization-dependent operation," *IEEE Trans. Antennas Propag.*, vol. 69, no. 3, pp. 1383-1392, Mar. 2021.

[11] X. Liu, Z. Yan, E. Wang, X. Zhao, T. Zhang and F. Fan, "Dual-band orthogonally-polarized dual-beam reflect-transmit-array with a linearly polarized feeder," *IEEE Trans. Antennas Propag.*, vol. 70, no. 9, pp. 8596-8601, Sept. 2022.

[12] J. Feng *et al*., "Reflect–transmit-array antenna with independent dual circularly polarized beam control," *IEEE Antennas Wireless Propag. Lett*., vol. 22, no,1. pp. 89–93, Jan. 2023.

[13] L.-X. Wu, K. Chen, T. Jiang, J. Zhao and Y. Feng, "Circular-polarization-selective metasurface and its applications to transmit-reflect-array antenna and bidirectional antenna," *IEEE Trans. Antennas Propag.*, vol. 70, no. 11, pp. 10207-10217, Nov. 2022.

[14] T. Cai, G.-M. Wang, X.-L. Fu, J.-G. Liang and Y.-Q. Zhuang, "High-efficiency metasurface with polarization-dependent transmission and reflection properties for both reflectarray and transmitarray," *IEEE Trans. Antennas Propag.*, vol. 66, no. 6, pp. 3219-3224, Sept. 2022.

[15] J. L. Wu, Y. M. Pan and S. Y. Zheng, "Design of single-layer polarization-dependent transmissive and reflective focusing metasurface," *IEEE Trans. Antennas Propag.*, vol. 69, no. 11, pp. 7637-7646, Nov. 2021.

[16] M. Wang, S. Xu, F. Yang and M. Li, "A 1-bit bidirectional reconfigurable transmit-reflect-array using a single-layer slot element with PIN diodes," *IEEE Trans. Antennas Propag*., vol. 67, no. 9, pp. 6205-6210, Sept. 2019.

[17] H. Yu, P. Li, J. Su, Z. Li, S. Xu and F. Yang, "Reconfigurable bidirectional beam-steering aperture with transmitarray, reflectarray, and transmit-reflect-array modes switching," *IEEE Trans. Antennas Propag*., vol. 67, no. 9, pp. 6205-6210, Sept. 2022.

[18] Y. Cao, W. Yang, Q. Xue and W. Che, "A broadband low-profile transmitarray antenna by using differentially driven transmission polarizer with true-time delay," *IEEE Trans. Antennas Propag.*, vol. 70, no. 2, pp. 1529-1534, Feb. 2022.

[19] J. Zhu, Y. Yang, S. Liao and Q. Xue, "Dual-band antenna hybridizing folded transmitarray and folded reflectarray," *IEEE Trans. Antennas Propag.*, vol. 70, no. 4, pp. 3070-3075, April. 2022.

[20] A. Freni, A. Mazzinghi and G. Carluccio, "Folded reflectarray with spherical polarizer," *IEEE Trans. Antennas Propag.*, vol. 68, no. 5, pp. 3613-3624, May. 2020.

[21] P. Mei, G. F. Pedersen and S. Zhang, "Performance improvement of mechanically beam-Steerable transmitarray antennas by using offset unifocal phase symmetry," *IEEE Trans. Antennas Propag.*, vol. 71, no. 1, pp. 1129-1134, Jan. 2023.

[22] J. Hu, H. Wong and L. Ge, "A circularly-polarized multi-beam magneto-electric dipole transmitarray with linearly-polarized feeds for millimeter-wave applications," *IEEE Trans. Antennas Propag*., vol. 70, no. 7, pp. 6012-6017, Jul. 2022.

[23] K.-M. Luk and H. Wong, "A new wideband unidirectional antenna element," *Int. J. Microw. Opt. Technol*., vol. 1, no. 1, pp. 35–44, Jun. 2006.

[24] X. Dai, X. Li and K. -M. Luk, "A planar wideband millimeter-wave antenna array with low sidelobe using '±1' excitations," *IEEE Trans. Antennas Propag.*, vol. 69, no. 10, pp. 6999-7004, Oct. 2021.

[25] Z. Xu, J. Li, and T. Yuan, "A full Ka-band compact coax-to-waveguide transition with shaped internal profile and enhanced fabrication process fexibility," in *Proc. IEEE Radio Wireless Symp. (RWS)*, Jan. 2022, pp. 26-29.
[26] B. Munk, *Finite Antenna Arrays and FSS*. New York: Wiley, 2003.
[27] S. S. Holland and M. N. Vouvakis, "The planar ultrawideband modular antenna (PUMA) array," *IEEE Trans. Antennas Propag.*, vol. 60, no. 1,pp. 130–140, Jan. 2012.
[28] Y.-M. Cai et al., "A novel ultrawideband transmitarray design using tightly coupled dipole elements," *IEEE Trans. Antennas Propag.*, vol. 67, no. 1, pp. 242-250, Jan. 2019.
[29] J. Zhu, Y. Yang, N. Hu, S. Liao, and J. Nulman, "Additively manufactured multi-material ultrathin metasurfaces for broadband circular polarizatioin decoupled beams and orbital angular momentum generation," *ACS Appl. Mater. Interfaces*, vol. 13, no. 49, pp. 59460-59470, 2021.
[30] J. Zhu et al., "Additively manufactured millimeter-wave dual-band single-polarization shared aperture Fresnel zone plate metalens antenna," *IEEE Trans. Antennas Propag.*, vol. 69, no. 10, pp. 6261-6272, Oct. 2021.
[31] M. Li, Y. Yang, F. Iacopi, J. Nulman, and S. Chappel-Ram, "3D-printed low-profile single-substrate multi-metal layer antennas and array with bandwidth enhancement," *IEEE Access*, vol. 8, pp. 217370–217379, 2020.
[32] F. Diaby, A. Clemente, R. Sauleau, K. T. Pham and L. Dussopt, "2 bit reconfigurable unit-cell and electronically steerable transmitarray at Ka-band," *IEEE Trans. Antennas Propag*., vol. 68, no. 6, pp. 5003-5008, Jun. 2020.
[33] X. Wang, P. -Y. Qin, A. Tuyen Le, H. Zhang, R. Jin and Y. J. Guo, "Beam scanning transmitarray employing reconfigurable dual-layer Huygens element," *IEEE Trans. Antennas Propag*., vol. 70, no. 9, pp. 7491-7500, Sep. 2022.